Thermalization of electrons in decaying extreme ultraviolet photons induced low pressure argon plasma

Thermalization of electrons in decaying extreme ultraviolet photons induced low pressure argon plasma

2016 Plasma Sources Sci. Technol. 25 035010

(http://iopscience.iop.org/0963-0252/25/3/035010)

IOP Publishing Plasma Sources Science and Technology

Plasma Sources Sci. Technol. **25** (2016) 035010 (8pp) doi:10.1088/0963-0252/25/3/035010

Thermalization of electrons in decaying extreme ultraviolet photons induced low pressure argon plasma

J Beckers[1], R M van der Horst[1], E A Osorio[2], G M W Kroesen[1] and V Y Banine[1,2]

[1] Eindhoven University of Technology, Den Dolech 2, 5612 AZ Eindhoven, The Netherlands
[2] ASML, De Run 6501, 5504 DR Veldhoven, The Netherlands

E-mail: j.beckers@tue.nl

Received 7 September 2015, revised 19 February 2016
Accepted for publication 10 March 2016
Published 6 April 2016

Abstract

We monitored—in the pressure range: 0.5–15 Pa—the electron temperature in decaying plasmas induced in argon gas by pulsed irradiation with extreme ultraviolet (EUV) photons with wavelengths closely around 13.5 nm. For this purpose, temporal measurements of the space-averaged and electric field weighted electron density after pulsed EUV irradiation are combined with an ambipolar diffusion model of the plasma. Results demonstrate that electrons are thermalized to room temperature before the plasma has fully expanded to the chamber walls for pressures of 3 Pa and higher. At pressures below 3 Pa, the electron temperature was found to be up to 0.1 eV above room temperature which is explained by the fact that plasma expansion is too quick for the electrons to fully thermalize. The comparison between plasma expansion duration towards a surface, plasma decay at a surface and time needed for thermalization and cooling of electrons is essential for designers of EUV lithography tools and EUV sources since the temperature of electrons dictates many fundamental physical processes.

Keywords: EUV, plasma, microwave cavity resonance spectroscopy, electron density, temperature

(Some figures may appear in colour only in the online journal)

1. Introduction

In view of the optical life-time of highly delicate and expensive multilayer mirrors in extreme ultraviolet (EUV) photolithography tools, characterization of the plasma induced by photoionization of a low pressure background gas by EUV photons is essential. To the end of shrinking semi-conductor structures, industry strives to apply photolithography with shorter and shorter wavelengths. Currently, the era of EUV lithography at 13.5 nm has begun and the transition into this era has already been discussed extensively in many publications starting in the late nineties [1]. Besides a whole new technology was to be developed to produce this EUV light, it is the technological necessity to operate the full tool in a low pressure background gas (0.5–15 Pa) rather than in high vacuum conditions, that recently introduced additional challenges. Due to the relatively large photoionization cross sections of the operational gases (i.e. argon or hydrogen) at the used wavelength of 13.5 nm [2–6], EUV induced plasma is created everywhere the beam travels in the tool, as first reported by Van der Velden *et al* [7, 8]. Background reason for industrial carefulness and the urge to fundamentally understand and reveal this exotic type of plasma, is the expected interaction of the induced plasma with the set of highly delicate multilayer mirrors (and other sensitive surfaces) and the unknown long term impact on operational processes. The expected interaction is due to the creation of a plasma sheath and consequently of high electric fields accelerating positive ions towards the surface. The resulting continuous ion bombardment may impact performance on time scales in the same order as the tool's specified lifetime, i.e. 5–10 years. In space, plasmas induced by photo-ionization are often referred to as

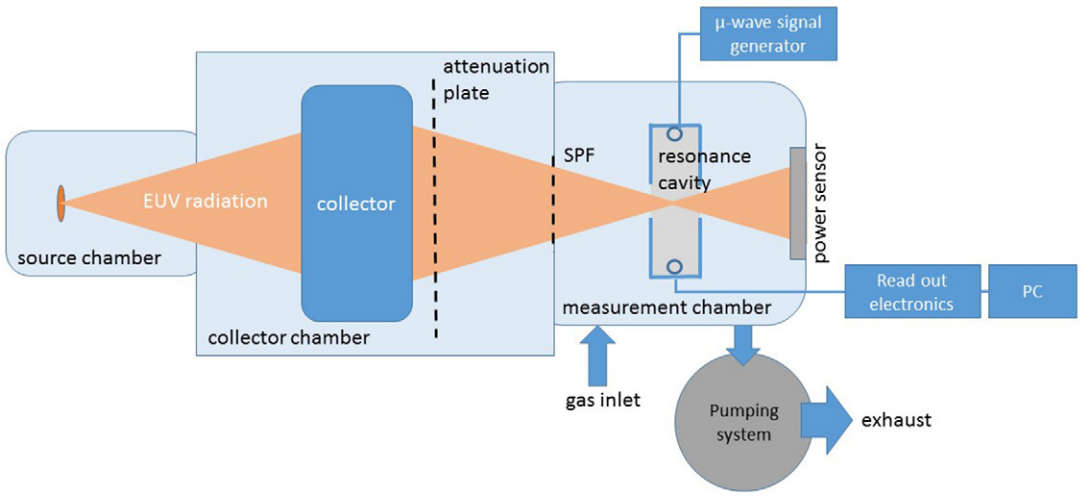

Figure 1. Schematic overview of the used experimental configuration with the source chamber, the collector chamber and the measurement chamber housing the resonant cavity for MCRS diagnostics and the EUV power sensor.

diffuse ionized gas (DIG) or warm ionized medium. In these cases, photons with a broad energy range from soft x-rays to VUV irradiated by stars, supernovae, etc, ionize interstellar clouds of gas, mainly hydrogen. These plasmas have been observed in all directions through the Milky Way [9] and have been subject to investigation for a long period. Research into these phenomena in space has been limited to optical experimental studies [10–12] and numerical simulations [13–16]. However, direct detection of electrons and their density and temperature is impossible in space and therefore the experiments presented in this work might be of interest to the astrophysical community as well.

Although multi-photon ionization of low pressure gases by means of irradiation with intense laser pulses has been researched on laboratory scales [17, 18], it was not until a decade ago—and at those times driven by industrial needs—that fundamental research on single-photon ionization of gases by photons in the EUV range started. Computer simulations and first experiments using Langmuir probes were performed by Van der Velden *et al* to determine one of the most important parameters, i.e. the electron density, to describe EUV induced plasmas in lithography tool conditions [7, 8]. In the view of experimentally determining densities of free electrons in the induced plasma, those authors concluded that Langmuir probes were not feasible, at least for this specific purpose. In reaction to that, van der Horst *et al* [19, 20] were in 2014 the first to introduce the utilization of a non-invasive technique based on microwave cavity resonance spectroscopy (MCRS) where the EUV induced plasma was created on the axis of a cylindrical resonant cavity. Although MCRS has been applied successfully to several other types of plasma configurations and plasma sources as well [21–27] and has demonstrated its feasibility to be a sensitive diagnostics for EUV induced plasmas [19, 20], the technique delivered solely information about the spatially averaged density of free electrons in the plasma, rather than information about the spatial distribution of electrons and about another important plasma parameter: the electron temperature.

The latter is tackled by developments presented in this contribution: we present by substantially developing the MCRS diagnostics for the first time measurements of the electron temperature in the decay phase of an EUV induced plasma. To achieve so, first, the technique is applied for longer time scales to monitor plasma dynamics after the plasma has expanded to the wall. Second, the MCRS diagnostics is combined with an ambipolar diffusion model. Third, relevant time scales for plasma expansion, electron-neutral collisions and electron–electron collisions are compared explain the observed trends. In this contribution, we explore thermalization of electrons during the decay of an EUV-induced plasma is presented.

2. Experimental configuration and method

The full experimental configuration consists of several parts (see figure 1) and has been discussed earlier in [19, 20]. Therefore, we suffice with only a brief description of the key features here and direct the reader to the references cited above.

The source chamber houses a pulsed Xenon-based discharge produced plasma (DPP) EUV source, generating pulsed EUV radiation with a pulse duration of 100–200 ns, a repetition rate of 500 Hz and pulse energies to be varied between 1 and 150 μJ per pulse (in-band: 10–20 nm) by using an attenuation plate. This source is based on generating EUV radiation by means of intense plasma heating due to the magnetic pinching effect. The operation principles and specifications of this source are extensively described by Bergmann *et al* [28]. The collector chamber houses a concentrically aligned set of elliptical and hyperbolic grazing incidence mirrors focussing the EUV light in the 'intermediate focus (IF)', located in the measurement chamber. The approximate radius of the EUV bundle in IF is $R_{\text{bundle}} = 2$ mm. A spectral purity filter (SPF), transmitting radiation between 10 nm and 20 nm only, separates the collector chamber and the measurement chamber and prevents irradiation of the measurement chamber by radiation with wavelengths larger than 20 nm. The measurement chamber with an argon background pressure between 0.5 Pa and 15 Pa houses an aluminum cylindrical resonant cavity

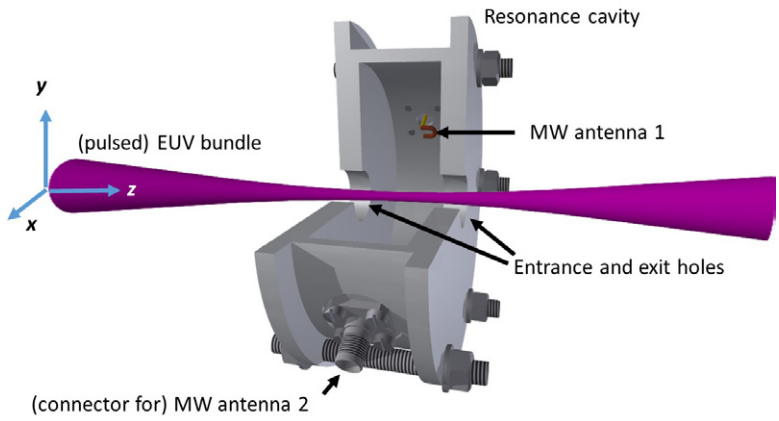

Figure 2. Schematics of the cylindrical resonant cavity containing two holes in top and bottom lids for entrance and exit of the EUV bundle. In the side walls of the cavity two antennas are mounted, one for excitation of the resonant mode, the other to monitor the cavity's response to that.

with an inner radius of $R_{cav} = 33$ mm and an inner height of 20 mm which is aligned around the IF (see figure 2). Top and bottom lids of the cavity contain holes—13 mm in diameter—for entrance and exit of the EUV light without irradiating any of the cavity walls. The latter to prevent photo-emission of electrons from the cavity wall material. Before, during and after an EUV pulse, the resonant frequency of an excited resonant mode is monitored as a function of time. A power sensor, being extensively described in [19, 20] measures the energy per pulse. All measurements presented in this contribution have been performed using the same EUV pulse energy of (53 ± 3) μJ.

2.1. MCRS

Microwave Cavity Resonance Spectroscopy (MCRS) is based on the principle that the resonant frequency of an excited mode in a resonant cavity depends—among others—on the permittivity of the medium inside this cavity. The permittivity on its turn is altered upon the creation of free electrons, making monitoring the response (in terms of resonant frequency) of the cavity to irradiation with EUV photons and subsequent ionization events an ideal diagnostics for the creation and dynamics of free electrons in the cavity volume. I.e. the presence of free electrons shifts the resonant frequency of individual resonant modes excited inside the resonant cavity and the temporal shift in resonant frequency can be related directly to the space averaged (over the cavity volume) and local square electric field $E(x)$ (of the resonant mode) weighted electron density $\tilde{n}_e$ (for a more detailed derivation see [21–27]) by:

$$\tilde{n}_e \equiv \frac{\iiint_{cav} n_e(x)E^2(x)d^3x}{\iiint_{cav} E^2(x)d^3x} \quad (1)$$

In the current work, the TM_{010} mode (see figure 3 for the mode's electric field distribution in the z-direction) has been used with a resonant frequency around $f = 3.482$ GHz.

Generally speaking, the detection limit of the MCRS technique is strongly connected to the quality factor Q, which is defined as the resonant frequency divided by the full with half max (FWHM) of the resonant peak in the frequency domain. For very high values of Q, the resonant peak is extremely narrow in the frequency domain. Consequently, very small deviations of the permittivity from its value in vacuum—and therefore also very small changes in electron density—can be detected resulting in an extremely low detection limit. However, a disadvantage of applying a high quality factor in MCRS is the poor temporal resolution, since the fundamental response time τ_{mcrs} of the cavity to changes in permittivity is connected to Q as: $\tau_{mcrs} = Q/\pi f$. In conclusion, with respect to resolution in (changes in) electron density one should strive for a highest possible Q factor, while with respect to the highest possible time resolution, a low value for Q would be desirable. In that framework—and to be able to follow the short time scales in EUV induced plasmas—the Q factor has been kept, by purpose, as low as 166, giving a best possible time resolution of 15 ns. The corresponding detection limit for the cavity averaged electron density—as can be observed from figure 4—is 5×10^{12} m^{-3}.

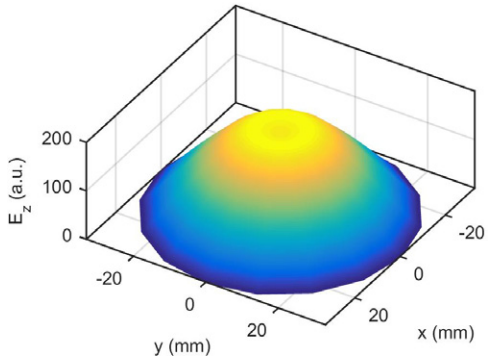

Figure 3. Calculated values of the E_z-component of the applied resonant mode TM_{010}. The z-direction is along the propagation velocity of the light in the EUV bundle (see figure 2) and the x- and y-direction are perpendicular to both the z-direction and each other.

3. MCRS plasma decay measurements

Van der Horst *et al* [19, 20] recently demonstrated the capability of MCRS to monitor the time-evolution of the space-averaged

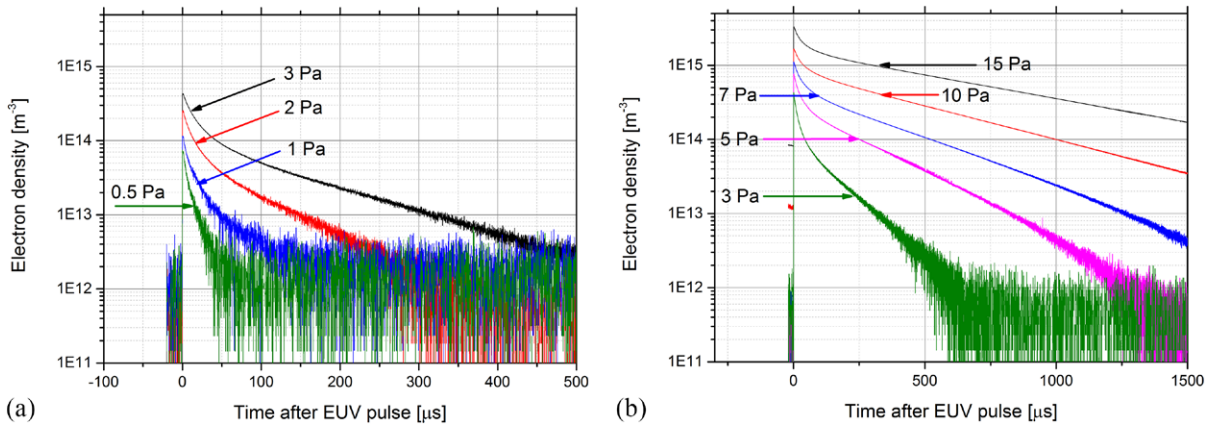

Figure 4. $\tilde{n}_e$ inside the resonant cavity as a function of time after a pulse of EUV light was directed through the cavity for background gas pressures of (a) 0.5 Pa to 3 Pa and (b) 3 Pa to 15 Pa. Pulse energy for all measurements was (53 ± 3) μJ and repetition rate of the source was 500 Hz.

density of free electrons created inside a resonant cavity by irradiation of a low pressure background gas with pulsed EUV radiation. Figures 4(a) and (b) show the plasma creation and decay in argon gas in terms of measured electron density $\tilde{n}_e$ at gas pressures ranging from 0.5 to 15 Pa and as a function of time after a pulse of EUV light was directed through the cavity. Note that—strictly speaking—time $t = 0$ is defined as the moment on which the EUV emission intensity is at its maximum value. For all measurements the pulse energy of the EUV pulses and the repetition rate of the source were kept constant at (53 ± 3) μJ and 500 Hz respectively. As can be observed from these figures, lower values of the electron density are measured at lower gas pressures. Since these values as closer to the detection limit (5×10^{12} m^{-3}) the measurements at low pressures contain more noise.

In this section we first explain qualitatively the behaviour of the cavity averaged electron density—especially at pressures above 2 Pa. In the next sections, we explore the influence of the gas pressure in a more quantitative fashion using an ambipolar diffusion model.

From the temporal evolution of the electron density, one can distinguish a plasma creation phase and two plasma decay phases. The two latter phases are denoted with 'Phase I' and 'Phase II' respectively (see figure 5 for a pressure of 15 Pa). The creation of the plasma occurs at much shorter time scales not visible on the time scale in figure 5 and is not the scope of the current contribution.

From the start of the EUV pulse, the curves plotted in figures 4(a), (b) and 5 can be described physically as follows: During the plasma creation phase, the electron density increases suddenly within typical time scales of hundreds of nanoseconds primary due to the creation of electrons by photoionization of the background gas and secondary followed by electron impact ionization which becomes more dominant at higher pressures. While the ions remain at room temperature, it is especially during this phase that the electrons have a high energy around 76 eV ($h\upsilon$ (@ 13.5 nm)—15.76 eV (ionization potential of argon)) and are strongly non-Maxwellian. On relatively short time scales (estimated later in this manuscript), the electron energy distribution function (EEDF) becomes

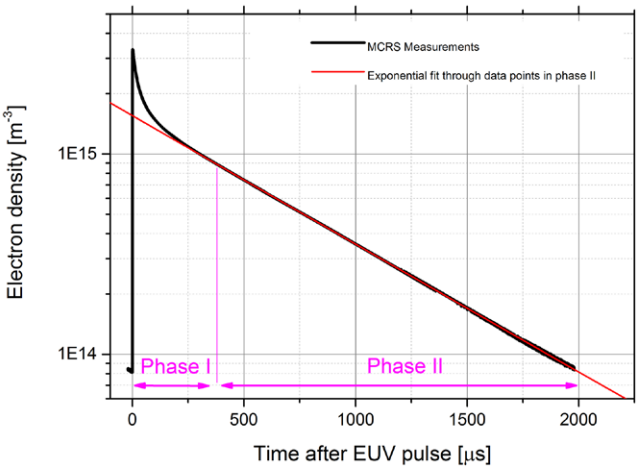

Figure 5. $\tilde{n}_e$ inside the resonant cavity as a function of time after a pulse of EUV light was directed through the cavity. Pulse energy was (53 ± 3) μJ, gas pressure was 15 Pa and repetition rate of the source was 500 Hz.

Maxwellian due to electron–electron collisions and the electron temperature starts to decrease due to electron-neutral collisions. Also, on these short time scales, a certain fraction of the fast electrons escapes towards the wall due to which an electric field is created pointing from the centre of the discharge to the cavity wall, confining electrons and accelerating positive ions towards the wall. In the first phase of the decay, i.e. 'Phase I', there is a rapid decrease in electron density with typical time scales of hundreds of microseconds. The observed decrease is not exponential—but faster—for which the reason is twofold:

(i) From the beginning of this phase—typically on time scales in the order of the inverse plasma ion frequency—ions start to be dragged along with the expanding electron cloud, i.e. ions and electrons start expanding outwards jointly. This alters the electron density distribution and also the extent (scaling with the square of the local electric field of the excited resonant mode (see figure 3)) to which these electrons are sampled by MCRS.

(ii) During the expansion phase, the electron temperature is not constant but decreases due to cooling.

At the beginning of 'Phase II', later in this manuscript indicated as 'onset time Phase II', the plasma has fully expanded to the cavity's walls and—in relative sense—a steady state spatial electron density distribution is developed. From this moment onwards, the joint transport of plasma species (electrons and positive ions) towards the cavity's walls is governed by ambipolar diffusion while—once at the wall—these species are subject to wall recombination. Note that the pressure and plasma densities applied here are sufficiently low to safely neglect (three-body) recombination processes in the cavity volume [20]. As can be seen in 'phase II' in figure 5, ambipolar diffusion at constant electron temperature followed by wall recombination of plasma species is—as one would expect—indeed governed by an exponential decay of the plasma density. It is the aforementioned 'Phase II' that is key in the current contribution and during which we are interested in the temperature of free electrons.

4. Ambipolar diffusion model

In order to derive the electron temperature in the decaying EUV induced plasmas, the experimentally determined electron density curves (see figure 4) are used in concert with the model discussed in this section. With ambipolar diffusion towards the wall and consequently followed by wall recombination being the only relevant loss channel for electrons and no significant electron production sources on these time scales [20], one expects the electron density to decrease exponentially as:

$$n_e(t) = n_e(0)\exp\left(-\frac{D_a}{\Lambda^2}t\right) \tag{2}$$

with Λ the typical diffusion length for cylindrical geometry as introduced by [29]

$$\frac{1}{\Lambda^2} = \left(\frac{\pi}{L}\right)^2 + \left(\frac{2.405}{R}\right)^2, \tag{3}$$

and D_a the ambipolar diffusion coefficient given by:

$$D_a = \frac{\mu_i D_e + \mu_e D_i}{\mu_i + \mu_e}, \tag{4}$$

with μ_i and μ_e the ion- and electron mobility respectively and D_i and D_e the diffusion coefficients for ions and electrons respectively. Applying the Einstein relations $D_{i,e} = \mu_{i,e} k_B T_{i,e}$ (with k_B the Boltzmann constant and T_i and T_e the ion and electron temperature respectively) and realizing that the electron mobility is much larger than the ion mobility ($\mu_e \gg \mu_i$), equation (4) can be rewritten to:

$$D_a = \mu_i(\widehat{T}_i + \widehat{T}_e). \tag{5}$$

Here, $\widehat{T}_i$ and $\widehat{T}_e$ are the ion and electron temperatures respectively being expressed in units of electron volt (eV). $\widehat{T}_i$ is assumed to equal room temperature, while the argon ion mobility is given by $\mu_i = \mu_i^0\left(\frac{10^5}{p}\right)$ [30] with $\mu_i^0 = 1.5 \times 10^{-4}$ m^2 (V s)$^{-1}$ [31]. Here, p is the gas pressure in units of Pa. Note that the derivation and equations above are valid only if local electron and ion densities are equal ($\overline{n}_e \approx \overline{n}_i$), i.e. at high values of induced plasma densities. However, for lower induced plasma densities—for instance at lower pressures—the initial escape of electrons may introduce a local positive space charge sufficiently significant for the ambipolar diffusion coefficient to be corrected as derived in [32]. However, for typical plasma densities and chamber geometries as observed and used in this work, the Debye length is much smaller than the plasma size and therefore the influence of space charge can safely be neglected.

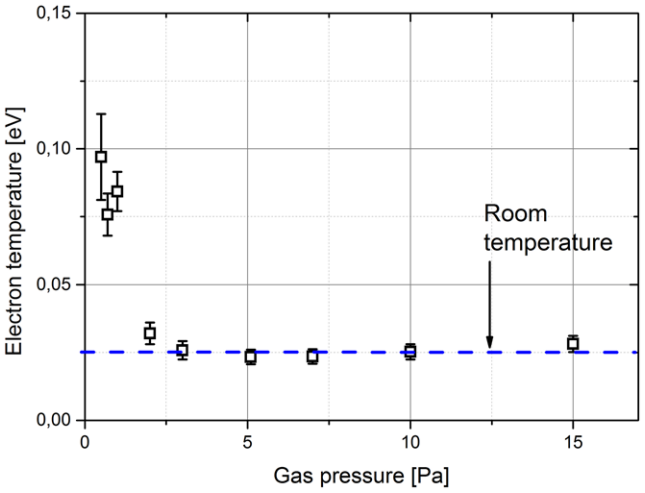

Figure 6. Electron temperature during the plasma decay phase (Phase II) as a function of gas pressure.

In order to eventually obtain the value of the electron temperature $\widehat{T}_e$, the curves in figure 4 in the domain where ambipolar diffusion dominates (i.e. as denoted as 'Phase II' in figure 5) are fitted with an exponential function. From this fit, a typical decay time scale τ is obtained which must equate the typical ambipolar time scale expressed as Λ^2/D_a. With known Λ (here 5.8 mm) one can easily calculate D_a and subsequently—via equation (5)—the value of $\widehat{T}_e$.

5. Results and discussion

Figure 6 shows the determined values for the electron temperature. From this figure, it can immediately be concluded that, within the error bars, this temperature equals room temperature (denoted with the dashed line) for pressures of 3 Pa and higher. This means that after the initiation of the EUV induced plasma, the electrons cool down within several hundreds of microsecond to room temperature. At pressures below 3 Pa, the found temperatures are slightly (up to ~0.1 eV) higher than room temperature.

In order to gain more insight in the physics behind the elevated electron temperatures at gas pressures below 3 Pa, we compare three relevant time scales with one another:

(I) the onset time for phase II (table 1) during which the plasma decays through ambipolar diffusion of plasma species to the wall followed by wall recombination,

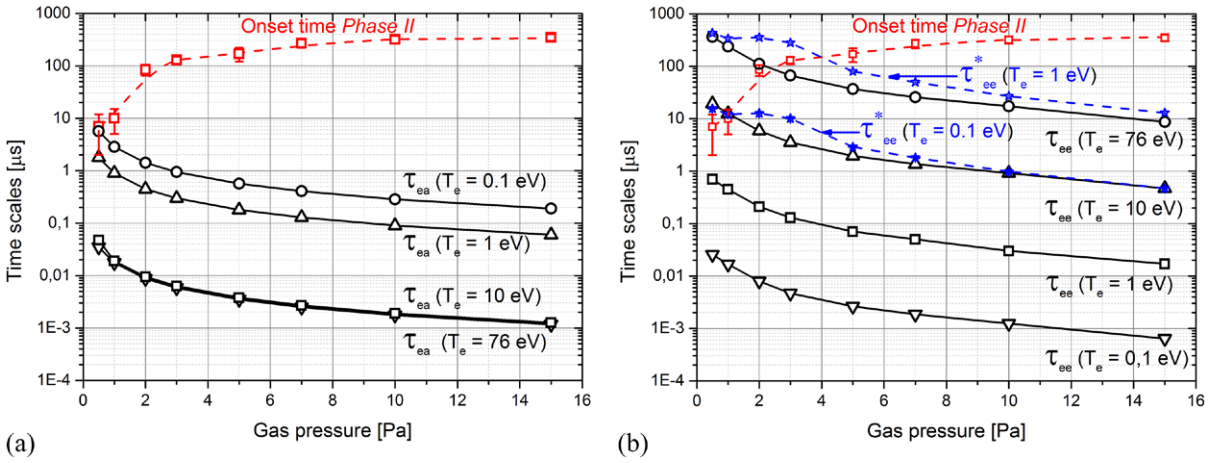

Figure 7. Onset time of 'Phase II' for several values of the background pressure compared to (a) the typical time scale for electron-neutral collisions, with $\sigma_{ea}\,(76\,\mathrm{eV}) = 5.9 \times 10^{-20}\ \mathrm{m}^{-2}$ [20] $\sigma_{ea}\,(10\,\mathrm{eV}) = 1.2 \times 10^{-19}\ \mathrm{m}^{-2}$ [34] and $\sigma_{ea}\,(1\,\mathrm{eV}) = \sigma_{ea}\,(0.1\,\mathrm{eV}) = 1 \times 10^{-20}\ \mathrm{m}^{-2}$ [34] and b) the typical time scale for electron–electron collisions where the values of τ_{ee} (black symbols, solid lines) have been calculated using the $\tilde{n}_e^{max}$ data in table 1 and the values of τ_{ee}^* have been calculated using the $\tilde{n}_e^{PhaseII}$ data in table 1.

Table 1. The local electron density $\tilde{n}_e^{max}$ just after the EUV pulse has been directed through the cavity, the onset time for Phase II and the averaged electron density $\tilde{n}_e^{PhaseII}$ at the beginning of Phase II for several relevant values of the gas pressure.

Gas pressure (Pa)	$\tilde{n}_e^{max}$ (10^{17} m^{-3})	Onset time 'Phase II' (μs)	$\tilde{n}_e^{PhaseII}$ (10^{15} m^{-3})
0.5	0.20 ± 0.02	7 ± 5	0.029 ± 0.003
1	0.32 ± 0.03	10 ± 5	0.037 ± 0.004
2	0.68 ± 0.07	85 ± 20	0.027 ± 0.003
3	1.1 ± 0.1	130 ± 20	0.045 ± 0.005
5	2.1 ± 0.2	175 ± 50	0.16 ± 0.02
7	3.0 ± 0.3	270 ± 50	0.26 ± 0.03
10	4.5 ± 0.5	320 ± 50	0.49 ± 0.05
15	9.1 ± 0.9	350 ± 50	1.0 ± 0.1

(II) the electron-neutral collisional time scale (figure 7(a)) providing information about electron cooling, and

(III) the electron–electron collisional time scale providing information about Maxwellisation of the EEDF (figure 7(b)).

The electron-neutral collisional time τ_{ea}, is calculated from:

$$\tau_{ea} = \frac{1}{n_a \sigma_{ea}} \sqrt{\frac{m_e}{k_B T_e}} \tag{6}$$

with m_e the mass of an electron, n_a the gas density and σ_{ea} the electron temperature dependent cross section for electron-neutral collisions. τ_{ea} is calculated for four values of the electron temperature, i.e. 76 eV (the maximum energy electrons can have after photoionization with 13.5 nm EUV photons), 10 eV, 1 eV and 0.1 eV. Comparing with the onset time for 'Phase II' in figure 7(a), one observes that τ_{ea} (35–50 ns) is more than two orders of magnitude shorter for electron temperatures of 76 eV and 10 eV while τ_{ea} is several times shorter at 1 eV and comparable with the onset time for 'Phase II' at 0.1 eV. Apparently, the electrons cool down to values below 1 eV very quickly, after which the cooling rate becomes increasingly longer for lower temperatures and becomes comparable to the onset time for 'Phase II'. This—as can be observed from figure 7(a)—applies to the low pressure case. At pressures above 3 Pa one can see that even at electron temperatures of 0.1 eV, τ_{ea} is sufficiently short to promote further cooling towards room temperature before 'Phase II' sets in.

Another time scale that needs to be considered is the electron–electron collisional time scale τ_{ee}, which can be estimated by [33]:

$$\tau_{ee} = \frac{6\sqrt{2}\,\pi^{3/2}\varepsilon_0^2\sqrt{m_e}\,(k_B T_e)^{3/2}}{e^4 n_e \ln \xi}, \tag{7}$$

with

$$\xi = \frac{12\pi\varepsilon_0 (k_B T_e)^{3/2}}{\sqrt{n_e}\, e^3} \tag{8}$$

For reasonable estimates of τ_{ee}, the value of $\tilde{n}_e$ must be chosen wisely and therefore we consider two limit situations.

First, the situation shortly after the EUV pulse has created the plasma. At this moment, the induced plasma has the same size as the EUV bundle (in the cavity). Hence, to obtain the local plasma density $\tilde{n}_e^{max}$ in the center at this moment, the measured cavity averaged electron density $\tilde{n}_e$ shortly after the EUV pulse should be multiplied by a factor $R_{cav}^2/R_{bundle}^2 \approx 272$ (see equation (1)). For several relevant values of the gas pressure, the experimentally determined value for $\tilde{n}_e^{max}$ is summarized together with the onset time for Phase II in table 1.

Second, at longer time scales the electron have cooled down significantly due to collisions with neutrals and the plasma as a whole has expanded towards the wall. Because of the very short time scales of 35–50 ns for τ_{ea} at 76 eV and 10 eV (see figure 7(a)), only τ_{ee} values for low electron temperatures (1 eV and 0.1 eV) are relevant and also the value of $\tilde{n}_e$ must be calculated for situations where the plasma has already expanded. In the limit case we use for the calculations the value of $\tilde{n}_e$ averaged over the full cavity at the start

of Phase II. The used measurement data are summarized in table 1 as well. Figure 7(b) shows—besides the onset time for Phase II—the value of τ_{ee} as a function of gas pressure for the relevant values of the electron temperature (where $\tilde{n}_e^{max}$ is used). For 1 eV and 0.1 eV, τ_{ee}^* has been calculated at the beginning of Phase II (where $\tilde{n}_e^{Phase\ II}$ is used).

In conclusion, just after the EUV pulse created the plasma, the plasma is confined within the volume of the EUV bundle and the energy of the electrons (at instance non-Maxwellian) is high (76 eV). At very short time scales (~50 ns), the temperature of the electrons decreases to values below 1 eV. As can be seen from figure 7(a), especially at low values of the gas pressure, typical times for electron cooling (τ_{ea}) become in the same order as the onset time for Phase II which explains the observed electron temperatures above room temperature in the order of 0.1 eV. As can be seen in figure 7(b), for pressures above 3 Pa, the typical time scales for electron–electron collisions are always significantly below the onset time for Phase II justifying the assumption of a Maxwellian EEDF during application of the ambipolar diffusion model.

6. Conclusion

The temperature of electrons in a plasma induced by irradiation of the argon background gas with EUV photons and decaying in a cylindrical resonant cavity has been estimated from temporally resolved measurements of the electrons density measured with microwave cavity resonance spectroscopy in concert with an ambipolar diffusion model. Electron temperatures close to room temperature have been found at pressures of 3 Pa and above, while at pressures below 3 Pa the electron temperature appeared slightly higher with values up to 0.1 eV. Reason for this behaviour of that electrons do not have sufficient time to thermalize before the plasma has expanded to the wall. The full plasma dynamics and the comparison between plasma expansion duration towards a surface, plasma decay at a surface and the time needed for thermalization and cooling of electrons is essential for designers of EUV lithography tools and EUV sources since the electron temperature dictates many fundamental physical processes, i.e. the energy of ions impinging the surface depends significantly on the electron temperature. Parameters to alter the involved physical processes are for instance gas pressure, repetition rate, pulse energy and type of gas.

Acknowledgments

The authors acknowledge ASML for measurement time on their EUV source and for their financial support.

References

[1] Parker A 1999 *EUVL Progress Report* S&TR November 1999
[2] Saito N and Suzuki I H 1992 Multiple photoionization in Ne, Ar, Kr and Xe from 44 to 1300 eV *Int. J. Mass Spectrom. Ion Process.* 157–72
[3] Möbus B, Magel B, Schartner K H, Langer B, Becker B, Wildberger M and Schimoranzer H 1993 Measurements of absolute Ar 3S photoionization cross sections *Phys. Rev.* A **47** 3888–93
[4] Dujardin G, Besnard M, Hellner L and Malinovitch Y 1975 Double photoionization of H_2: an experimental test of electronic-correlation models in molecules *Phys. Rev.* A **35** 5012–9
[5] Chung Y M, Lee E M, Masuoka T and Samson J A R 1993 Dissociative photoionization of H_2 from 18 to 124 eV *Chem. Phys.* **99** 885
[6] Kossmann H, Schwarzkopf O, Kammerling B, Braun W and Schmidt V 1989 Photoionization cross section of H_2 *J. Phys. B: At Mol. Opt. Phys.* **22** L411
[7] Van der Velden M H L, Brok W J M, Van der Mullen J J A M, Goedheer W J and Banine V Y 2006 Particle-in-cell Monte Carlo simulations of an extreme ultraviolet radiation driven plasma *Phys. Rev.* E **73** 036406
[8] Van der Velden M H 2008 *PhD Thesis* Eindhoven University of Technology
[9] Haffner L M, Reynolds R J, Tufte S L, Madsen G J, Jaehnig K P and Percival J W 2003 The Wisconsin Halpha Mapper Northern Sky Survey *Astrophys. J. Suppl.* **149** 405
[10] Haffner L M, Reynolds R J and Tufte S L 1999 Wham observations of H alpha, (S II), and (N II) toward the orion and perseus arms: probing the physical conditions of the warm ionized medium *Astrophys. J.* **523** 223
[11] Savage B D and Wakker B P 2009 The extension of the transition temperature plasma into the lower galactic halo *Astrophys. J.* **702** 1472–89
[12] Gaensler B M, Madsen G J, Chatterjee S and Mao S A 2008 The vertical structure of warm ionised gas in the Milky Way *PASA* **25** 184–200
[13] Miller W W and Cox D P 1993 The diffuse ionized interstellar-medium—structures resulting from ionization by O-stars *Astrophys. J.* **417** 579
[14] Wood K and Mathis J S 2004 Monte Carlo photoionzation simulations of diffuse ionized gas *MNRAS* **353** 1126
[15] Ciardi B, Bianchi S and Ferrara A 2002 Lyman continuum escape from an inhomogeneous interstellar medium *MNRAS* **331** 463
[16] Wood K, Hill A S, Joung M R, Mac Low M-M, Benjamin R A, Haffner L M, Reynolds R J and Madsen G J 2010 Photoionization of high-altitude gas in a supernova-driven turbulent interstellar medium *Astrophys. J.* **721** 1397
[17] Hughes V and Grabner L 1950 The radiofrequency spectrum of RBF-85 and RBF-87 by the electric resonance method *Phys. Rev.* **79** 314–22
[18] Mainfray G and Manus C 1991 Multiphoton ionization of atoms *Rep. Prog. Phys.* **54** 1333–72
[19] Van der Horst R M, Beckers J, Nijdam S and Kroesen G M W 2014 Exploring the temporally resolved electron density evolution in extreme ultra-violet induced plasmas *J. Phys. D: Appl. Phys.* **47** 302001
[20] Van der Horst R M, Beckers J, Osorio E A and Banine V Y 2015 Exploring the electron density in plasmas induced by extreme ultraviolet radiation in argon *J. Phys. D: Appl. Phys.* **48** 285203
[21] Haverlag M, Kroesen G M W, Bisschops T and De Hoog F J 1991 Measurement of electron-densities by a microwave cavity method in 13.56 MHz RF plasmas of Ar, CF_4, C_2F_6 and CHF_3 *Plasma Chem. Plasma Process.* **11** 357–70
[22] Kroesen G M W, Stoffels W W, Stoffels E, Haverlag M, de Boer J H W G and de Hoog F J 1994 Negative ions and particle formation in low-pressure halocarbon discharges *Plasma Sources Sci. Technol.* **3** 246–51
[23] Beckers J, Stoffels W W and Kroesen G M W 2009 Temperature dependence of nucleation and growth of nanoparticles in low pressure Ar/CH_4 RF discharges *J. Phys.* D **42** 155206-1–10

[24] Beckers J and Kroesen G M W 2011 Surprising temperature dependence of the dust particle growth rate in low pressure Ar/C_2H_2 plasmas *Appl. Phys. Lett.* **99** 181503
[25] Van de Wetering F M J H, Beckers J and Kroesen G M W 2012 Anion dynamics in the first 10 milliseconds of an argon-acetylene radio-frequency plasma *J. Phys. D: Appl. Phys.* **45** 485205
[26] Beckers J and Kroesen G M W 2013 Gas temperature dependence of coagulation onset times for nanoparticles in low pressure hydrocarbon plasmas *Appl. Phys. Lett.* **103** 123106–9
[27] Van de Wetering F M J H, Brooimans R J C, Nijdam S, Beckers J and Kroesen G M W 2015 Fast an interrupted expansion in cyclic void growth in dusty plasma *J. Phys. D: Appl. Phys.* **48** 035204
[28] Bergmann K, Rosier O, Lebert R, Neff W and Poprawe R 2001 A multi-kilohertz pinch plasma radiation source for extreme ultraviolet lithography *Microelectron. Eng.* **57–8** 71–7
[29] Luikov A 1968 *Analytical Heat Diffusion Theory* (New York: Academic)
[30] Ellis H, Pai Y, McDaniel E W, Mason E A and Viehland L A 1976 Transport properties of gaseous ions over a wide energy range *At. Data Nucl. Data Tables* **17** 177–210
[31] Helm H and Elford M T 1977 The mobility of Ar^+ ions in argon and the effect of spin/orbit coupling *J. Phys. B: At. Mol. Phys.* **10** 3849–51
[32] Rogoff G F 1985 Ambipolar diffusion coefficients for discharges in attaching gases *J. Phys. D: Appl. Phys.* **18** 1533–45
[33] Golant V E, Zhilinsky A P and Sakharov I E 1980 *Fundamentals of Plasma Physics* (New York: Wiley)
[34] Franz G 2009 *Low Pressure Plasmas and Microstructuring Technology* (Dordrecht: Springer)